Optical Engineering

SPIEDigitalLibrary.org/oe

Self-spectral calibration for spectral domain optical coherence tomography

Xianling Zhang
Wanrong Gao
Haiyi Bian
Chaoliang Chen
Jiuling Liao

SPIE

Self-spectral calibration for spectral domain optical coherence tomography

Xianling Zhang
Nanjing University of Science and Technology
Department of Optical Engineering
200 Xiao Ling Wei
Nanjing, Jiangsu 210094, China
and
Nanjing University of Information and Science Technology
School of Physics and Optoelectronic Engineering
Nanjing, Jiangsu 210044, China

Wanrong Gao
Haiyi Bian
Chaoliang Chen
Jiuling Liao
Nanjing University of Science and Technology
Department of Optical Engineering
200 Xiao Ling Wei
Nanjing, Jiangsu 210094, China
E-mail: gaowangrong@yahoo.com

Abstract. A different real-time self-wavelength calibration method for spectral domain optical coherence tomography is presented in which interference spectra measured from two arbitrary points on the tissue surface are used for calibration. The method takes advantages of two favorable conditions of optical coherence tomography (OCT) signal. First, the signal back-scattered from the tissue surface is generally much stronger than that from positions in the tissue interior, so the spectral component of the surface interference could be extracted from the measured spectrum. Second, the tissue surface is not a plane and a phase difference exists between the light reflected from two different points on the surface. Compared with the zero-crossing automatic method, the introduced method has the advantage of removing the error due to dispersion mismatch or the common phase error. The method is tested experimentally to demonstrate the improved signal-to-noise ratio, higher axial resolution, and slower sensitivity degradation with depth when compared to the use of the zero-crossing method and applied to two-dimensional cross-sectional images of human finger skin. [DOI: 10.1117/1.OE.52.6.063603]

Subject terms: optical coherence tomography; spectral domain; self-spectral calibration; interferometer.

Paper 130336 received Mar. 5, 2013; revised manuscript received May 21, 2013; accepted for publication May 23, 2013; published online Jun. 19, 2013.

1 Introduction

Spectral domain optical coherence tomography (SDOCT) is a noninvasive, noncontact imaging modality,[1–4] in which the depth profile of the tissue is retrieved by performing inverse Fourier transform of the interference signal generated by the light back-scattered from the interior of the sample. The light reflects from the reference mirror in a Michelson interferometer configuration. SDOCT has the advantages of wider dynamic range and higher signal-to-noise ratio (SNR) than the time-domain implementation.[5] One limitation of SDOCT is that the spectrum is sampled uniformly in wavelength and unevenly sampled in wavenumber space (k-space) which leads to variations of the axial resolution and the image quality along with the axial or A-scan direction. Hence, accurate calibration of the spectrum is necessary to obtain high quality SDOCT cross-sectional images.[6]

Several methods have been proposed for spectrum calibration. One calibration method is based on a specially designed spectrometer that linearly samples the wavenumber.[7–9] This method reduces post-processing needs but complicates system design. The other direct calibration methods proposed include a characteristic wavelength method[10] and a spectral interferogram mapping method,[11,12] which are based on directly measuring part of the wavelength distribution on the charge-coupled device (CCD) by standard equipment and then performing polynomial fitting to obtain the wavelength alignment on the whole CCD pixels. The need of external devices such as an external light source with known spectral features or a well-calibrated commercial optical spectrum analyzer (OSA) increases system complicity and cost. In Refs. 13 and 14, calibration methods without the need of external devices were proposed. In these methods, the wavelength assignments are obtained with the help of the linear relationship between phase or phase difference of interference spectra and the wavenumber on CCD. However, they need separate measurement steps which may cause errors in calibration data because of environmental temperature fluctuation effects on the system or poor stability of handling practices. For the need of real-time imaging, a real-time or adaptive calibration routine is necessary. Mujat et al proposed a self-calibration method in which the intensity spectrum of the light source is modulated by an external sinusoidal signal in k-space with a thin glass slide inserted at the exit of the light source.[15] Liu et al proposed an automatic spectrometer calibration method in which an accurate estimation of wavenumber assignment on CCD was obtained by adopting zero-crossing detection technique.[16] Since the differences in wavenumbers between any two adjacent zero-crossing points are identical, by finding out all the zero-crossing points, the wave numbers at these zero-crossing points are known up to a scaling factor and an offset. Then spectrometer calibration can be realized through polynomial fitting process. The algorithm used in Ref. 16 is effective and simple and can achieve calibration with high precision. But this method is inherently unreliable in the cases where there are some large phase errors that arise from a large polarization mode dispersion mismatch between the reference arm and the sample arm, or when the phases of the calibration spectrum are contaminated by noises.

The automatic spectral calibration method presented here is based on two spectra that are from two different transverse positions of the tissue under observation. The use of the

spectra for calibration is based on the following favorable facts. First, the strength of signal back-scattered from most of the tissue surface is generally much stronger than from positions inside the tissue due to the large refractive difference at the surface, so the component of the surface interference could be extracted from the measurement spectrum and could be approximated to a specular interference spectrum. Second, the tissue surface is not a plane, so there is phase difference between the light reflected from two arbitrary transverse points on the surface.

2 Principle

A typical SDOCT system consists of a broadband light source such as super-luminescent diode (SLD), a Michelson interferometer and a spectrometer (see Fig. 1). The light from the SLD source is split into two beams and launched into two interferometer arms by a fiber coupler. They recombine and interfere in the detection arm after being reflected back from the reference reflector and back-scattered from the sample, respectively. The interference light is separated into monochromatic light in space and detected by a spectrometer. The interference signal composed by the three terms: the autocorrelation of the reference light, the autocorrelation of the sample light and their mutual interference term is recorded by the spectrometer and detected by the line-scan CCD. The mutual interference term of the output electric current of the line-scan CCD can be expressed as Eq. (1) with the system phase error taken into account[17]

$$I_m(\lambda) = \alpha S(\lambda) \sum_i R_i \cos\left[2\frac{2\pi}{\lambda} z_i + \beta(\lambda)\right], \tag{1}$$

where $S(\lambda)$ is the power spectrum of the light source, α is a constant related to the responsibility of the CCD, reflection loss in the reference and detection arms, $\beta(\lambda)$ denotes the phase error of the two arms and is a function of the wavelength, and R_i is the amplitude reflectance of the light at the interfaces within the tissue at the depth z_i. From Eq. (1) we can see that the interference spectrum can be considered as a weighted sum of a series of cosine signals with a different frequency z_i. The weighting factors are coefficients of R_i. For most tissues, the refractive index variation across the surface is generally much larger than that at positions in the tissue interior.[18] Hence, in spite of the complexity of the tissue, amplitude reflectance R_i near the surface is much greater than that of other depths.[18] When the digitized interference spectrum current is transferred to the computer and filtered by a band-pass digital filter with a centre frequency equal to the optical path difference (OPD) between the tissue surface and the reference mirror, approximately only the light reflected from the tissue surface is then obtained.

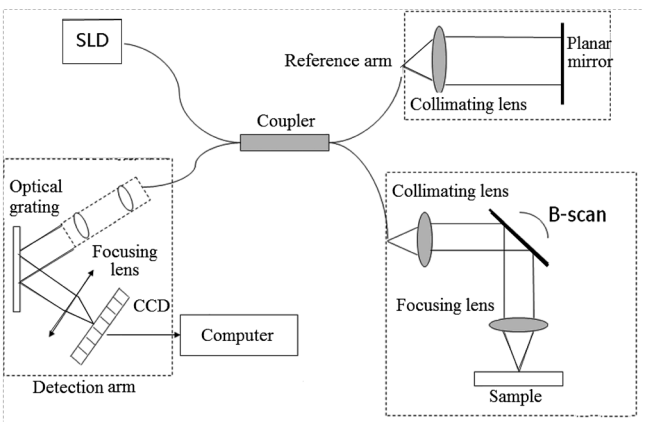

Fig. 1 Schematic of spectral domain optical coherence tomography system.

Before performing system spectrum calibration, direct inverse Fourier transforms were performed to all the interference spectra obtained at different transverse positions to form a two-dimensional (2-D) raw image. From the raw image, two of the interference spectra with different OPDs at the tissue surface in the spatial domain were chosen for calibration. The phases of the spectral signals were then extracted by performing Hilbert transform and further unwrapped. From Eq. (1), it can be seen that the phase of the spectrum can be expressed as

$$\phi_i(\lambda) = \frac{4\pi}{\lambda} z_i + \beta(\lambda). \tag{2}$$

Hence the phase difference $\Delta\phi(n)$ can be expressed as

$$\Delta\phi(n) = \phi_B - \phi_A = \frac{4\pi}{\lambda_n}\Delta z, \tag{3}$$

where Δz is the difference between OPDs from two points at the tissue surface, ϕ_A and ϕ_B are the phase distributions at the positions "A" and "B," respectively, and n is the CCD pixel index. Obviously, the phase error term $\beta(\lambda)$ has been canceled due to subtraction.

To facilitate the analysis, we introduce a phase difference function Δ_i by the formula

$$\Delta_i = \phi_i(\lambda_M) - \phi_i(\lambda_N), \tag{4}$$

where M and N denote the two different pixel indexes of the CCD. The difference of OPDs between positions "A" and "B" can be rewritten as

$$\Delta z = (T-1)\cdot z_A, \tag{5}$$

where $T = \Delta_B/\Delta_A = z_B/z_A$, z_A, and z_B are the OPDs of spectra at the positions "A" and "B," respectively. The values of M, N (M, $N <$ CCD pixels number) for "A" and "B" are then substituted into Eq. (3) to obtain each phase differences Δ_A and Δ_B and T. The value of Δz is not determined because z_A is unknown. Since z_A cannot be measured directly by the position of the maximum of the signal in spatial domain because of the position error induced by the direct inverse Fourier transform of the spectrum which is nonuniformly sampled in k-space. An initial value of z_A is chosen according to the position of signal maximum in spatial domain by direct inverse Fourier transform without calibration. Since a more accurate spectral calibration means a better OCT image sharpness,[19] we may decide the precise value of the z_A by an iterative algorithm by maximizing the sharpness of the reconstructed OCT A-scan.

When Δz is determined, the whole wavelength distribution on the CCD is determined up to λ_0 at the first pixel index on the CCD.

3 Experiment System and Results

In our experiment, an SLD with a centre wavelength of 834 nm and a bandwidth of 40 nm was used as the light source, corresponding to the theoretical coherence length 7.7 μm in air. A 2×2 50/50 fiber coupler splits the incident light beam into two beams. The detection arm consists of an achromatic collimating lens with a 60-mm focal length, a 1200-line/mm holographic grating, and an achromatic lens of 150-mm focal length for focusing the diffracted beam into the line-scan CCD camera that has 1024 pixels with a 14-μm pixel size, and a 12-bit digital resolution (e2v AViiVA SM2CL). The spectral resolution of the system that is determined by the CCD pitch length and the resolution of optical grating is 0.0674 nm, which gives a 2.59 mm maximum imaging depth in air. The spectra range covered by CCD is 69 nm.

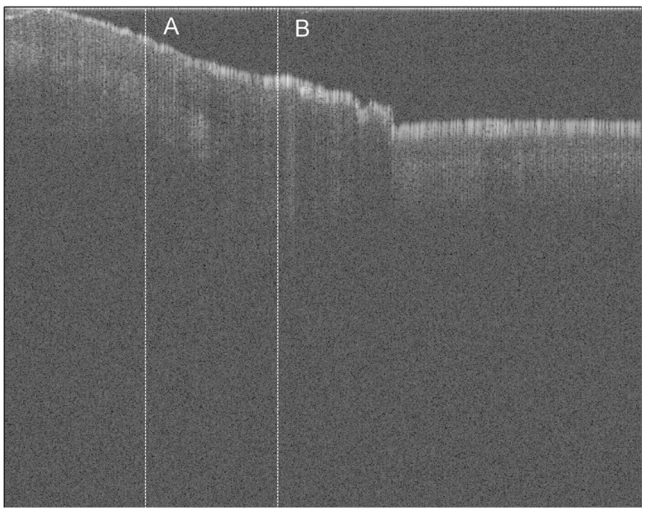

Fig. 2 Raw image of human skin at fingernail without spectral calibration. "*A*" and "*B*" denote the positions where the spectra were used for calibration.

The spectral data from CCD were converted and digitalized into digital signals and transferred to the computer by the image acquisition system. Then a one-dimensional (1-D) reflection distribution of the tissue along with the depth direction by inverse Fourier transform of the spectral data on the computer was obtained. Furthermore, by scanning the light beam across the tissue surface, the spectral data at different transverse positions were acquired and a 2-D tomographic image of the tissue was then generated by performing the inverse Fourier transform.

A raw cross-sectional image of a volunteer's finger skin was obtained with our experiment system (see Fig. 2). The spectra chosen for calibration are marked by "*A*" and "*B*" in Fig. 2 and are depicted in Fig. 3(a) and 3(b), respectively. The corresponding filtered interference spectra are shown in Fig. 3(c) and 3(d). Figure 3(e) and 3(f) show the amplitude spectra at positions "*A*" and "*B*," respectively, obtained with the sample replaced by a mirror. When Fig. 3(c) is compared with Fig. 3(e) or Fig. 3(d) is compared with Fig. 3(f), it can be seen that the fringe period of the filtered spectra at "*A*" and "*B*" are nearly equal to that obtained with the mirror, as sampled with the same OPD, respectively. It should be noted that the positions of "*A*" and "*B*" indicated in Fig. 2 can be any of the two positions in the image.

The unwrapped phase distributions of the filtered spectra and the wavelength distribution can be determined by the

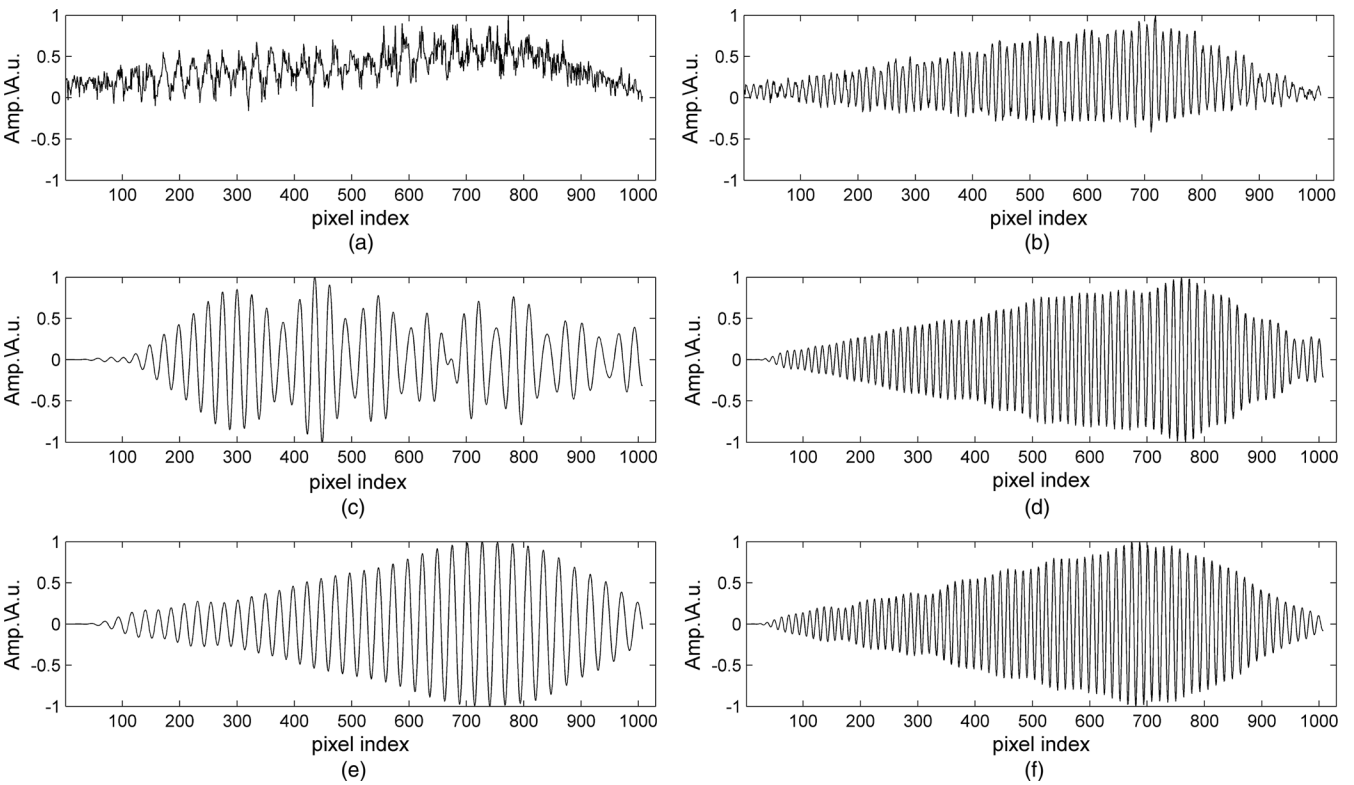

Fig. 3 Measured interference spectra corresponding to "*A*" (a) and "*B*" position (b); the corresponding filtered interference spectra for "*A*" (c) and "*B*" (d), respectively; and the spectra obtained by using mirror as the sample at positions "*A*" (e) and "*B*" (f).

procedure described in Sec. 2. The results are shown in Fig. 4. With these calculated wavelength distributions on CCD pixels, an interpolation and sequent inverse Fourier transform of the spectra of the volunteer's skin of a fingernail were carried out and a 2-D cross-sectional image with good quality was obtained, as shown in Fig. 5(b). For comparison, the image reconstructed without calibration is also given in Fig. 5(a). The zoomed-in views of two local areas in the two images marked by the rectangles were also overlying on the images. From the enlarged local images in Fig. 5(b), one can see that the human sweat glands, the skin surface, and the bottom layer of the fingernail can be clearly visualized after calibration.

4 Performance Analysis

4.1 *System SNR and Axial Resolution Improvement*

To quantitatively evaluate the performance of the presented calibration method, the SNRs and axial resolutions of the system with and without calibration were calculated. In the following analysis, the SNR is defined as[20]

$$\mathrm{SNR} = 20 \log \frac{I_{\max}}{\sigma}, \tag{6}$$

where $I_{\max}$ is the maximum of the signal intensity in spatial domain, σ is the background noise root-mean-square error. The axial resolution is defined as the full width at 3 dB less than the maximum of the point spread function (PSF). The interference spectra at several different OPDs when the sample was replaced by a mirror were measured. Inverse Fourier transforming of these interference spectra yield several 1-D signal distributions along with the depth direction that represent variations of the system PSF with depth. The SNRs and axial resolutions for the different OPDs were calculated by use of the obtained PSFs.

The PSFs of the system at different depths without calibration and with calibration are illustrated in Fig. 6(a) and 6(b). Then, the SNRs and axial resolutions at different depths

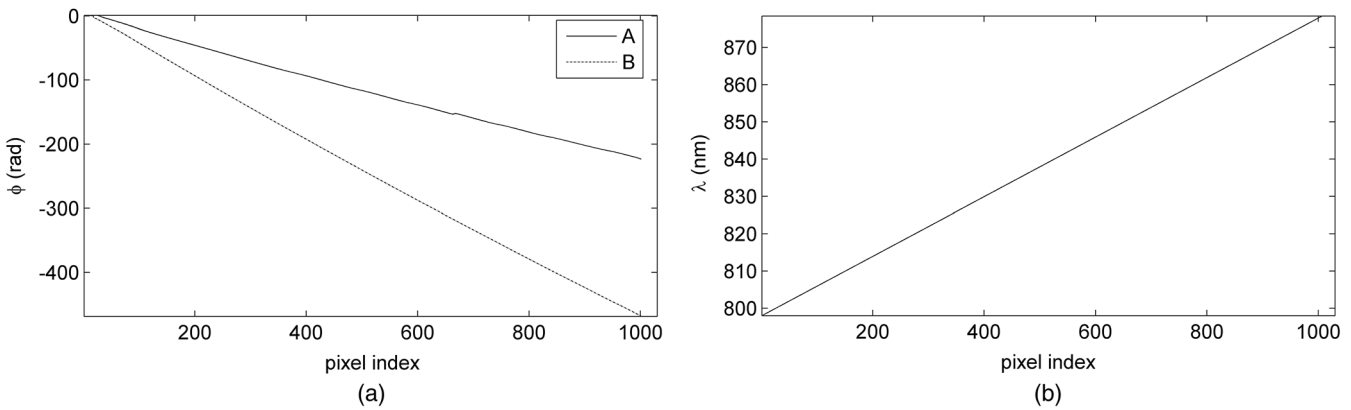

Fig. 4 The unwrapped phase distributions of the complex spectrum for position "*A*" and "*B*" (a) and the calculated wavelength distributions on CCD pixels (b).

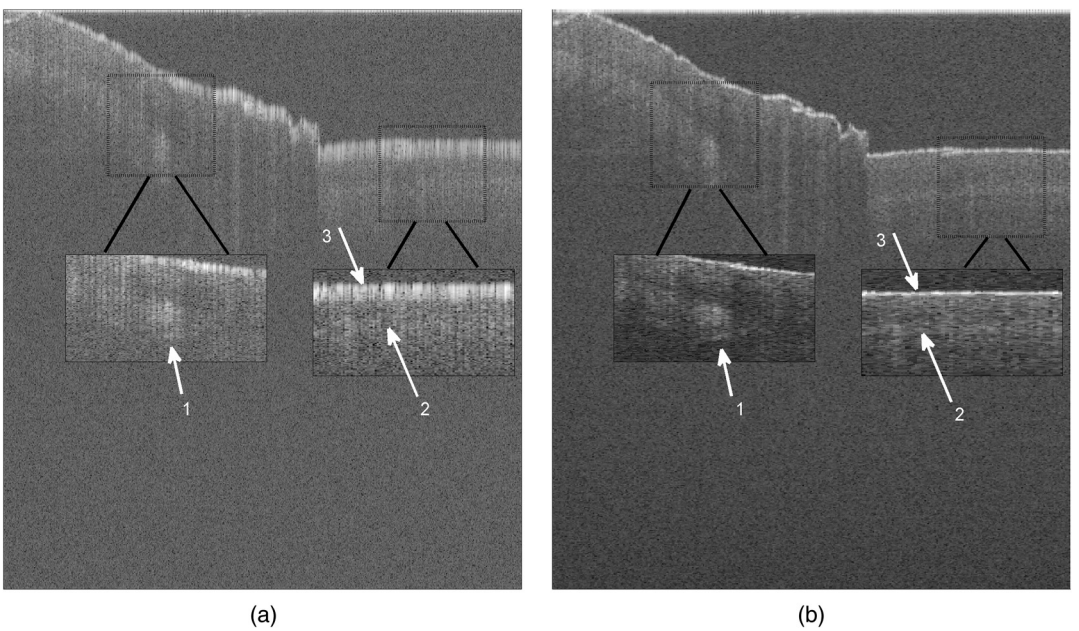

Fig. 5 Images of skin of fingernail without (a) and (b) with spectral calibration.

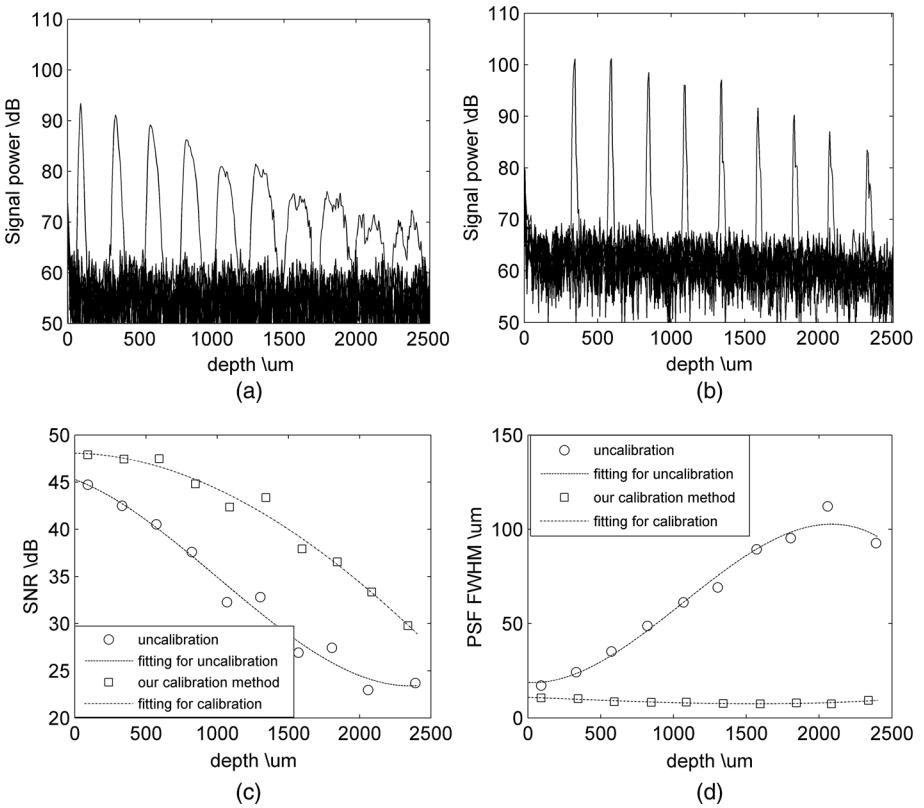

Fig. 6 (a) PSFs at different depths without calibration; (b) PSFs at different depths with calibration based on our method; (c) the fitting curve of SNR variations; and (d) the fitting curve of resolution versus depth (dot line and dash-dot line represent the results without and with calibration, respectively).

were calculated according to measured PSFs and a third-order polynomial fitting were applied to the calculated data, respectively [see Fig. 6(c) and 6(d)]. One can see that the SNR and the axial resolution of the system without calibration decrease greatly with depth. For comparison, the quadratic fitting coefficient and first-order fitting coefficient of the SNR fitting curve are −0.0003 and −0.037 for the uncalibrated system and −0.0001 and −0.003 for the calibrated system with the proposed self-calibration method, respectively. The cubic fitting coefficients are both less than 10 to the minus 7th power. These values indicate that the degrading speed of SNR has been halved after calibrating with our method.

The axial resolution of the uncalibrated system is about 50 μm at the depth of 1 mm, which is about five times larger than that at zero OPD and further deteriorates with depth [see Fig. 6(d), dotted line]. As a comparison, the averaged axial resolution of the calibrated system over the 2.5 mm range is close to the theoretical axial resolution and is almost unchangeable with the depth [see Fig. 6(d), dash-dotted line].

4.2 *Comparison with Zero-Crossing Method*

One advantage of our method over the zero-crossing method is that it has the capability of compensating the large phase errors.[16] To clearly demonstrate this fact, we analyzed the same unwrapped phase distributions denoted by "*A*" and "*B*" in Fig. 2 and calibrated the system with zero-crossing method without the complex optimization for fitting coefficients.[16]

To this end, first, the positions of the zero-crossing points are counted and plotted in Fig. 7(b). One can see from the Fig. 7(b) that a few zero-crossing points deviate from its true positions significantly. This may arise from some phase errors, as shown in Fig. 7(a) (black arrows). This fact shows that the phase errors in determining zero-crossing positions can affect the spectrum calibration precision further.

Using the zero-crossing calibration method with the spectra at "*A*" and "*B*," the 2-D cross-sectional images of the same finger skin were generated, respectively [see Fig. 8(a) and 8(b)]. Compared with the calibrated image in Fig. 5(b), it can be seen that although the image quality could be improved by the calibrating system with the zero-crossing method, the method presented in this paper is more effective with clearer boundaries.

The calculated PSFs corresponding to different OPDs of the calibrated system with the zero-crossing calibrating method with the spectra at "*A*" and "*B*" [see in Fig. 8(c) and 8(d)] further validate the above conclusions. The SNRs and axial resolutions for different OPDs and their fitting curves were calculated and drawn in Fig. 8(e) and 8(f) together with the results obtained by our method. Both the quadratic fitting and first-order fitting coefficients of the SNR curve obtained with the calibrated system by the spectrum at "*A*" are more than three times than that of the corresponding coefficients with our self-calibration and the corresponding coefficients of "*B*" are 1.8 times and one-tenth, respectively. The results show that our method has a stronger capability of suppressing the decline speed in SNR with depth than the zero-crossing method.

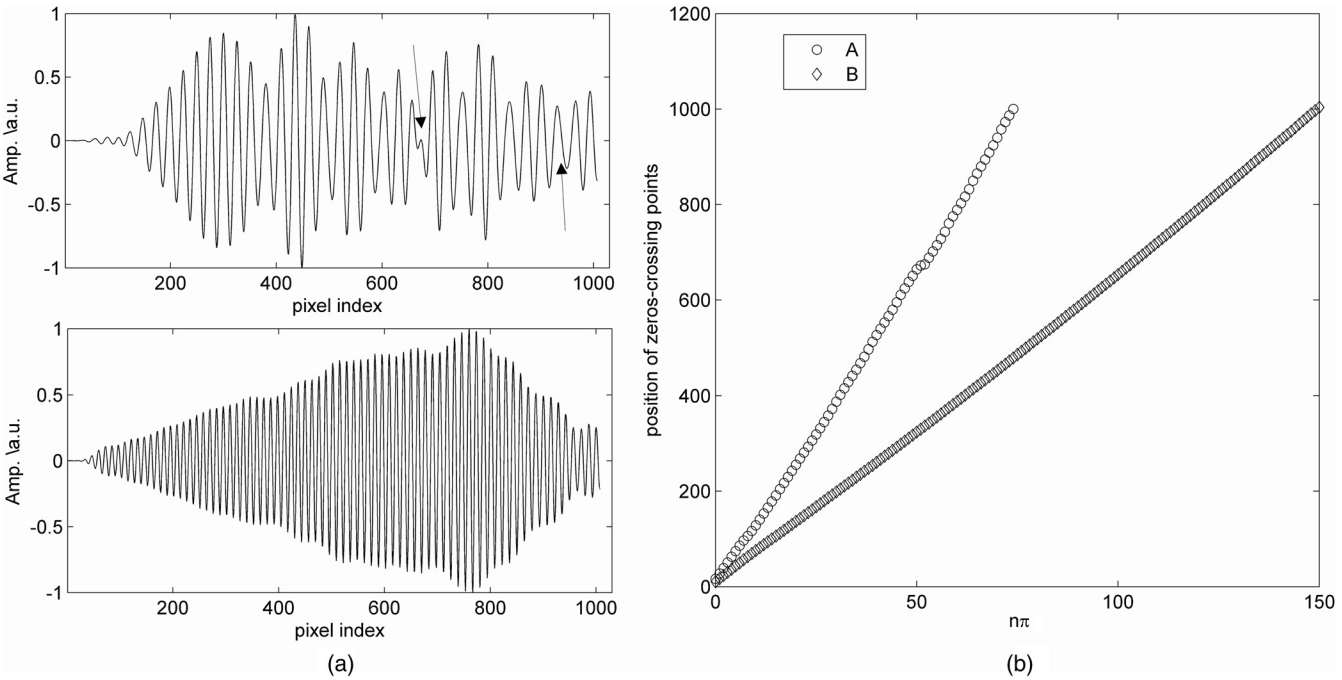

Fig. 7 (a) Filtered spectra for position "*A*" and (the above one) and "*B*"; (b) pixel index of the zero-crossing points with spectrum "*A*" (circle) and with spectrum "*B*" (diamond).

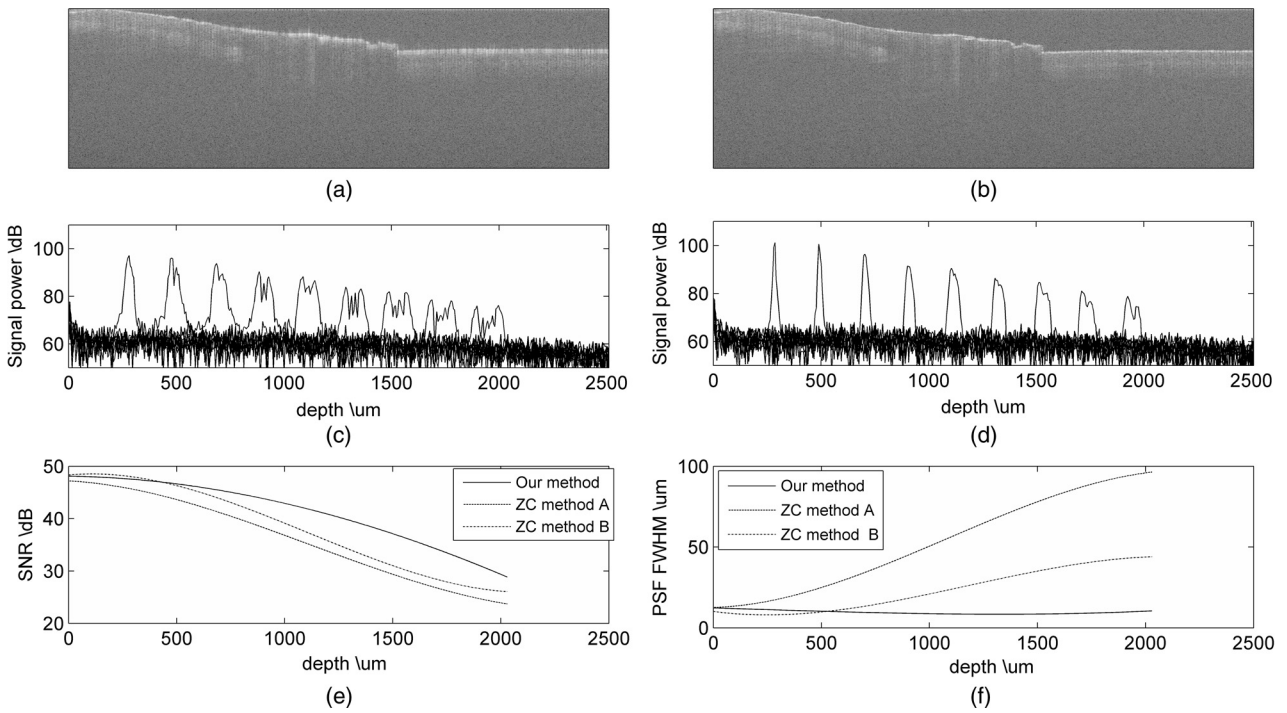

Fig. 8 (a, b) Reconstructed 2-D cross-sectional image with the zero-crossing method with spectrum "*A*" (a) and with spectrum "*B*" (b); (c, d) PSFs at different depths with the zero-crossing method with spectrum "*A*" (c) and with spectrum "*B*" (d); (e) SNRs comparison, and (f) resolution distributions versus depth for the three calibration results. (ZC is the abbreviation for zero-crossing.)

The average 3 dB width of the PSF for the zero-crossing method with the spectra at "*A*" and "*B*" at the depth of 2 mm are almost five times and three times wider than that obtained with our self-calibration method, respectively. Hence, our method has an advantage of improving the axial resolution of the system due to the fact that the phase errors in the interference spectrum signal are removed by subtraction of the two complex spectrum phases, so higher calibration precision can be achieved.

In addition, by comparison between the two calibration results obtained with spectrum at "*A*" and "*B*" with zero-crossing method, it shows that the spectrum "*B*" is more appropriate for calibration than the one at "*A*." Based on this analysis, we can see that the conditions are stricter for the

zero-crossing method to choose the appropriate spectrum for calibration.

5 Conclusions

An automatic calibration method which allows calibration for SDOCT system during scanning operation without external calibration light source and external measurement step is presented in this paper. The method allows choosing calibration spectrum from all the measurement spectra more randomly and can remove most of the phase error between the reference arm and the sample arm. There is also no need of a next fitting coefficient correction. Experimental results show that the axial resolution and depth sensitivity of the 2-D reconstructed images from spectral domain after calibration have been improved significantly.

Acknowledgments

This research was supported by the National Natural Science Foundation of China (61275198, 60978069). The authors thank the reviewers for their careful reading of the manuscript and insightful comments.

References

1. A. F. Fercher, "Optical coherence tomography," *J. Biomed. Opt.* **1**(2), 157–173 (1996).
2. M. Wojtkowski et al., "*In vivo* human retinal imaging by Fourier domain optical coherence tomography," *J. Biomed. Opt.* **7**(3), 457–463 (2002).
3. V. J. Srinivasan et al., "Depth-resolved microscopy of cortical hemodynamics with optical coherence tomography," *Opt. Lett.* **34**(20), 3086–3088 (2009).
4. L. An, J. Qin, and R. K. Wang, "Ultrahigh sensitive optical microangiography for *in vivo* imaging of microcirculations within human skin tissue beds," *Opt. Express* **18**(8), 8220–8228 (2010).
5. J. F. de Boer et al., "Improved signal-to-noise ratio in spectral-domain compared with time-domain optical coherence tomography," *Opt. Lett.* **28**(21), 2067–2069 (2003).
6. R. Leitgeb, C. K. Hitzenberger, and A. F. Fercher, "Performance of Fourier domain vs. time domain optical coherence tomography," *Opt. Express* **11**(8), 899–894 (2003).
7. Z. Hu and A. M. Rollins, "Fourier domain optical coherence tomography with a linear-in-wavenumber spectrometer," *Opt. Lett.* **32**(24), 3525–3527 (2007).
8. Z. Ning et al., "Spectral-domain optical coherence tomography with a Fresnel spectrometer," *Opt. Lett.* **37**(8), 1307–1309 (2012).
9. D. Choi et al., "Fourier domain optical coherence tomography using optical demultiplexers imaging at 60,000,000 lines/s," *Opt. Lett.* **33**(12), 1318–1320 (2008).
10. Y. Chen et al., "Densely folded spectral images of a CCD spectrometer working in the full 200–1000 nm wavelength range with high resolution," *Opt. Express* **13**(25), 10049–10054 (2005).
11. Z. Wang et al., "Increasing the imaging depth of spectral-domain OCT by using inter-pixel shift technique," *Opt. Express* **14**(16), 7014–7023 (2006).
12. C. Ding et al., "A new spectral calibration method for Fourier domain optical coherence tomography," *Optik* **121**(11), 965–970 (2010).
13. R. A. Leitgeb et al., "Ultrahigh resolution Fourier domain optical coherence tomography," *Opt. Express* **12**(10), 2156–2165 (2004).
14. K. Wang and Z. Ding, "Spectral calibration in spectral domain optical coherence tomography," *Chin. Opt. Lett.* **6**(12), 902–904 (2008).
15. M. Mujat et al., "Autocalibration of spectral-domain optical coherence tomography spectrometers for *in vivo* quantitative retinal nerve fiber layer birefringence determination," *J. Biomed. Opt.* **12**(4), 041205 (2007).
16. X. Liu et al., "Towards automatic calibration of Fourier-domain OCT for robot-assisted vitreoretinal surgery," *Opt. Express* **18**(23), 24331–24343 (2010).
17. P. H. Tomlins and R. K. Wang, "Theory, developments and applications of optical coherence tomography," *J. Phys. D* **38**(15), 2519–2535 (2005).
18. J. M. Schmitt and G. Kumar, "Optical scattering properties of soft tissue: a discrete particle model," *Appl. Opt.* **37**(13), 2788–2797 (1998).
19. M. Wojtkowski et al., "Ultrahigh-resolution, high-speed, Fourier domain optical coherence tomography and methods for dispersion compensation," *Opt. Express* **12**(11), 2404–2422 (2004).
20. D. Lian et al., "Development of a spectrum domain 3D optical coherence tomography system," *Chin. J. Lasers* **36**(10), 2528–2533 (2009).

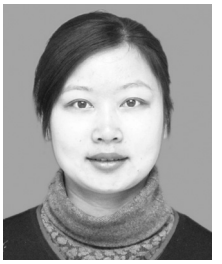

Xianling Zhang received her BS and MS degrees in optics engineering from Nanjing University of Science and Technology in 2001 and 2004, respectively. Since 2004, she has been a lecturer in the Nanjing University of Information and Science Technology and now she is studying for PhD in optics engineering in Nanjing University of Science and Technology. Her interests include optical signal detection and image processing.

Wanrong Gao received his PhD degree from Xi'an Institute of Optics and Fine Mechanics, Chinese Academy of Sciences in 1996. He worked as a post-doctor fellow in Nanjing University of Science and Technology from October 1996 to October 1998. He worked in a Professor Peter T. C. So's Laboratory at Massachusetts Institute of Technology from February 2002 to February 2003 and Professor Joseph A. Izatt's Laboratory at Duke University from March 2011 to March 2012, as a visiting scientist. Now he is a professor of the Department of Optical Engineering, Nanjing University of Science and Technology China. He conducts research in biomedical optics and spectroscopy.

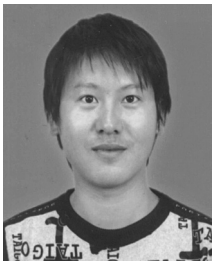

Haiyi Bian received his bachelor's degree in photoelectric information engineering from Nanjing University of Science and Technology in 2011. And now he is studying for his PhD in optics engineering in Nanjing University of Science and Technology. His research interest is biomedical imaging.

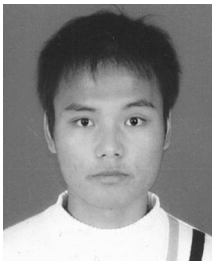

Chaoliang Chen received his bachelor's degree in photoelectric information engineering from Nanjing University of Science and Technology in 2011. Now he is currently completing his PhD in optics engineering in Nanjing University of Science and Technology. His research interests include biomedical optics and image processing.

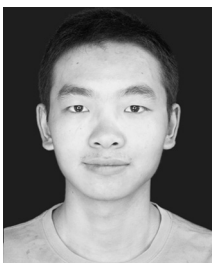

Jiuling Liao received his BS degree in photoelectric information engineering from Nanjing University of Science and Technology in 2012. Now he is studying for PhD in optics engineering in Nanjing University of Science and Technology. His research interests include biomedical imaging and spectral analysis.